Soil Dynamics and Earthquake Engineering 150 (2021) 106804

Contents lists available at ScienceDirect

Soil Dynamics and Earthquake Engineering

journal homepage: www.elsevier.com/locate/soildyn

Assessment of small-strain characteristics for vibration predictions in a Swedish clay deposit

Freddie Theland [a,*], Geert Lombaert [b], Stijn François [b], Costin Pacoste [a,d], Fanny Deckner [c], Jean-Marc Battini [a]

[a] Division of Structural Engineering and Bridges, KTH Royal Institute of Technology, Brinellvägen 23, 100 44, Stockholm, Sweden
[b] Department of Civil Engineering, KU Leuven, Kasteelpark Arenberg 40, 3001, Leuven, Belgium
[c] GeoMind KB, Hesselmans Torg 5, 131 54, Nacka, Sweden
[d] ELU Konsult AB, Valhallavägen 117, 115 31. Stockholm, Sweden

ARTICLE INFO

Keywords:
Environmental vibration
Dynamic soil properties
Clay
Surface waves
Topsoil

ABSTRACT

Environmental vibrations induced by human activities such as traffic, construction or industrial manufacturing can cause disturbance among residents or to vibration sensitive equipment in buildings. In Sweden, geological formations of soft clay overlying a stiff bedrock are soil conditions prone to ground vibrations that are encountered both in urban areas and along parts of the national railway network. This paper presents an extensive investigation of the small-strain soil properties for the prediction of environmental ground vibrations in a shallow clay where the bedrock is situated at 7.5 m depth. The small-strain properties are estimated using available empirical correlations, bender elements, seismic cone penetration tests, seismic refraction and inversion of surface wave dispersion and attenuation curves. The results are synthesised into a dynamic layered soil model which is validated by measurements at the soil's surface at source-receiver distances up to 90 m in the frequency range 1–80 Hz. Analyses of uncertainties in the estimated values of wave speeds and material damping are performed by model investigations, indicating that surface wave tests overestimate the damping compared to bender element tests. The properties of the topmost unsaturated part of the soil is found to have a significant influence on the response at large distances, caused by critically refracted P-waves resonating in the top layer.

1. Introduction

Human activities such as construction, industrial manufacturing processes or traffic on roads and railway can give rise to vibrations spreading to its surroundings through the soil. In the built environment, buildings located in the vicinity of vibration sources might experience excessive vibration levels, potentially leading to disruption in the operation of vibration sensitive equipment or discomfort for residents. For the assessment of ground borne vibrations in buildings, numerical or empirical models can be applied to predict building vibration levels prior to construction. The mechanical soil properties and the stratification at a site have a significant influence on the amplitude and frequency content of the dynamic response of the soil [1,2]. Therefore, numerical models require an estimation of these parameters while some empirical models directly make use of the free field surface responses at the prospective site [3,4].

Ground borne vibration emanating from railways is an important societal concern that is receiving an increasing amount of attention globally [5]. A number of studies have been focused on the validation of models to predict railway induced ground vibrations in the free field. In these studies, small-strain soil properties and layered soil models are obtained either from non-invasive geophysical methods, covering large volumes of soil, or in situ wave speed measurements taken at discrete points or over a smaller distance. Lombaert et al. [6] performed a validation of a numerical model for the prediction of railway induced vibrations in the free field. The validation study was performed in steps, separating the estimation of small-strain soil properties and the measurements of the track-free field responses and train passages, allowing to assess the propagation of errors in the prediction model. The results emphasized the large influence of the soil properties on the predicted free-field responses. Kouroussis et al. [7] validated a finite element model to compute the free field response in the time domain due to the passing of high speed trains. The layering of the soil at the site was shown to have a large influence on the frequency content of the

* Corresponding author.
E-mail address: freddie.theland@byv.kth.se (F. Theland).

https://doi.org/10.1016/j.soildyn.2021.106804
Received 23 November 2020; Received in revised form 27 April 2021; Accepted 30 April 2021
Available online 5 August 2021

predicted response. Connolly et al. [8] analysed ground borne vibration levels from measurement records at seventeen different sites along European railways. An assessment of the influence of train type, train speed and site conditions on the vibrations levels was undertaken. The site specific soil conditions were found to be the most influential aspect affecting the levels of ground borne vibration. In particular, the differences in vibration levels tended to increase with the distance from the track. These observations highlight the importance of correctly accounting for the soil conditions when constructing models to perform predictions of ground borne vibrations, especially with an increasing distance from the source.

Along the national railway tracks and in densely populated urban areas in Sweden, geological formations of soft clay deposits overlying till and a stiff bedrock are encountered. These type of soil conditions have been found to be prone to ground borne vibration problems [4,9,10]. The small-strain properties of Swedish clay soils have been studied extensively using laboratory measurements and seismic methods. Empirical relations have been established to determine the initial shear modulus for geotechnical engineering applications [11–13]. An extensive investigation of small-strain soil properties was performed in Ledsgård along the West-coast line between Göteborg and Malmö in Sweden, due to the exceptionally high amplitude of vibrations encountered at the railway track [14–16]. The properties were determined in the deep marine clay from both laboratory, invasive and non-invasive in situ measurements. Measured track and free field responses at frequencies below 5 Hz due to train passages could be numerically reconstructed using the identified soil properties [17,18].

Determination of the small-strain properties in Swedish clays has so far mainly been focused on the use for either track response or static small-strain deformation analyses. The analysis of environmental vibrations requires a representation of the soil that is able to predict the dynamic response at significant source-receiver distances. For practical applications project restrictions and budget constraints can limit the extent of site investigations available to estimate the small-strain properties. Therefore, it is important to understand the ability of different investigation methods to acquire the necessary information to perform accurate predictions with a dynamic soil model.

This paper presents an extensive geotechnical and geophysical site characterization of a Swedish clay deposit in the Stockholm area. The objectives of this paper are to investigate the ability to represent a clay deposit with a shallow bedrock by a linear elastic layered soil model for the prediction of environmental ground vibrations by synthesis of small-strain properties obtained from various site investigation methods and to compare their performance in acquiring the necessary properties.

The soil conditions at the site constitute a representative example of post-glacial clays encountered in Sweden, allowing extension of the presented conclusions to sites where similar conditions are encountered.

The small-strain properties of the soil are determined by empirical relations, invasive wave speed measurements and non-invasive geophysical investigation methods. The results are compared and a synthesis of the information provided by the investigations is made to establish a representative soil model. Parametric uncertainties in the estimated soil properties are identified their influence on the computed free field responses is investigated by numerical simulations and compared to measurements at different source-receiver offsets. Finally, response measurements at the soil's surface acquired during different seasons are presented to assess the influence of seasonal variations on the soil's dynamic response.

The outline of the paper is as follows. Section 2 presents the layout and general soil conditions of the site where the investigations are performed. Section 3 presents the results obtained from a geotechnical site investigation and an overview of the methods used to estimate the small-strain properties from both in situ tests and laboratory samples. Section 4 presents the setup and data processing of two measurement campaigns where frequency response functions are estimated along the soil's surface. These are used for model validation and non-invasive estimation of small-strain properties by seismic refraction and spectral analysis of surface waves (SASW) by inversion of dispersion and attenuation curves. In section 5, the small-strain properties obtained from different investigation methods are presented, compared and synthesised into a representative soil model. Section 6 presents a validation of the soil model and an analysis of the influence of remaining uncertainties on the soil properties on the predicted responses. Section 7 addresses the influence of seasonal variation on the soil's response. Finally, section 8 presents the conclusions of the paper.

2. Test site

The test site is located in Brottby, 40 km north of Stockholm, Sweden. The site is an agricultural field that has not been cultivated for more than ten years prior to the site investigations. The site is intended as a test site for experimental investigations on the small-strain dynamic behaviour of end-bearing pile foundations. It was chosen because of its particular stratification, with a soft clay underlain by till and bedrock, representative for soil conditions prone to high amplitudes of ground borne vibration, the potential to represent the soil with a layered soil model over the area of interest and that unlimited access to the site could be granted. As the site is located in a remote location, a minimum of outside disturbances is present during testing. Moreover, a designated site makes the placement of stationary reference points possible, allowing to compare measurements performed at different occasions to assess the influence of seasonal variations.

Fig. 1 presents an aerial view together with the locations of the performed site investigations.

Fig. 2 presents geological information of the soil deposits and the soil depth to bedrock [20]. The geological information gives an overview of the topography of the underlying bedrock at the site, suggesting that the field is positioned along a fracture zone in the bedrock, overlain by layers of till and clay. The site investigations are concentrated over an area in the center of the field where the estimated soil depth is 5–10 m, as presented in Fig. 1.

3. Invasive site investigations

3.1. Overview of site investigations

The positions where the invasive tests have been performed are presented in Fig. 1.

Penetration tests over the investigation area were performed to establish an interpretation of the stratigraphy on the site and in situ wave speeds were measured by SCPT. Samples of the clay were analysed in the laboratory, providing geotechnical parameters to perform empirical predictions of the small-strain soil properties, as well as estimates of wave speeds and material damping ratios from bender element tests.

3.2. Soil topography and stratification

In points P7–P12, weight soundings were performed to provide an overview of the general variation of the stratigraphy on the site. The weight sounding penetrates the softer soil layers, but cannot penetrate the stiffer non-cohesive soil. In P8 and P13, CPTU was performed in the clay giving an indirect interpretation of the layering at the site. In addition, disturbed samples were taken in points P11 and P13 to determine the soil types of the profile by visual inspection. Three plastic groundwater pipes of 76 mm diameter were installed down to the non-cohesive soil with a consecutive 1 m spacing in points P15–P17. Apart from measuring the ground water pressure levels, these sounding wells are also used to install multiple sensors in the soil for geophyscial tests. However, after pre-drilling the holes down to the bedrock, the pipes could not be pushed down further than 0.8 m into the non-cohesive soil due to collapse of the pre-drilled holes, preventing reliable cross- or

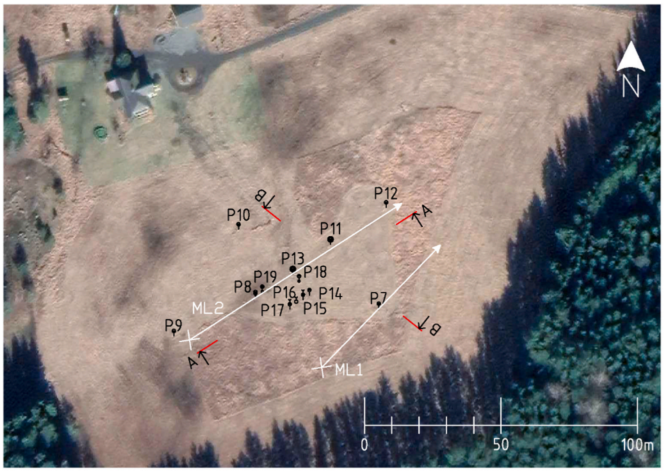

Point	Tests
P7	Ws
P8	Ws,SCPT,CPTU
P9	Ws
P10	Ws
P11	Ws,Scr
P12	Ws
P13	Scr,SCPT,CPTU,PS
P14	MWD
P15	MWD,Gwp
P16	MWD,Gwp
P17	MWD,Gwp
P18	MWD
P19	MWD

Fig. 1. Aerial photograph [19] of the test site with the geotechnical investigation points P7–P19 and measurement lines ML1 and ML2 along which dynamic measurements are performed due to applied hammer impacts ($\times$) superimposed. Tests performed at each point are listed in the accompanying table as weight soundings (Ws), screw samples (Scr), measurement while drilling (MWD), installation of ground water pipes (Gwp), piston samples (PS), seismic cone penetration test (SCPT) and cone penetration test with measurement of pore water pressure (CPTU).

down-hole measurements. Soil/rock probing was performed in points P18 and P19 to determine the depth to the bedrock. The test is commonly used in Sweden and is internationally referred to as measuring while drilling (MWD) described in the international standard ISO 22476-15 [21,22]. During the drilling, driving force, resistance, penetration speed, engine pressure, hammer pressure and flushing pressure are registered versus the penetration depth. This allows interpretation of layering of soils not penetrable by the CPT probe, identification of inclusions such as boulders and quality assessment of the bedrock. In point P14 pre-drilling was initiated for installation of a ground water pipe, but came to an early stop at a depth of 4 m, indicating the presence of a boulder or a local variation of the bedrock topography.

The collective information acquired from the in situ tests results in an interpreted soil profile presented in Fig. 3, illustrated in the sections A–A and B–B with reference to Fig. 1. The soil consists of layers of dry-crust clay, saturated clay and till on top of a stiff bedrock.

3.3. Seismic cone penetration tests

Two seismic cone penetration tests (SCPT) and regular CPTU tests were performed in the points P8 and P13. The spacing of the triaxial accelerometers installed in the CPT probe was 1 m. Each test was performed by hitting ribbed plates pre-loaded by the drill rig, presented in Fig. 4. The tests were performed with a depth interval of 0.5 m and in each test 10 hits were applied in two perpendicular directions in the front and the back of the rig. The wave speeds are estimated based on the difference in arrival time between the receivers calculated using time domain cross-correlation and assuming a straight travel path from the center of the plates to the receivers.

Each measurement is assigned a representative depth $z_{SCPT} = z_2(r_1 + r_2)/2r_2$, where z_j and r_j are the probe depth and radial distance from the source point for sensor j, respectively [23].

3.4. Laboratory tests

In P13, two sets of piston samples were collected for laboratory analysis at the levels 1–4 m in the clay. High quality samples were obtained using a category A method according to ISO 22475–1:2006 [24]. Table 1 presents the classification of the soil collected in the piston samples of the clay, made by visual inspection in the laboratory in accordance with international standards [25,26].

Laboratory investigations of the soil included determination of the soil's density ρ, the water content w, the liquid and plastic limits w_L and w_P yielding the plasticity index I_p, the sensitivity of the clay S_t, the undrained shear strength τ_{fu} determined from both triaxial and fall-cone tests and the over-consolidation ratio (OCR) obtained from oedometer tests with a constant rate of strain (CRS). The sensitivity, the plastic limit and the OCR could not be determined for the 1 m level consisting of dry-crust clay, possibly due to disturbance of the tested sample. The soil

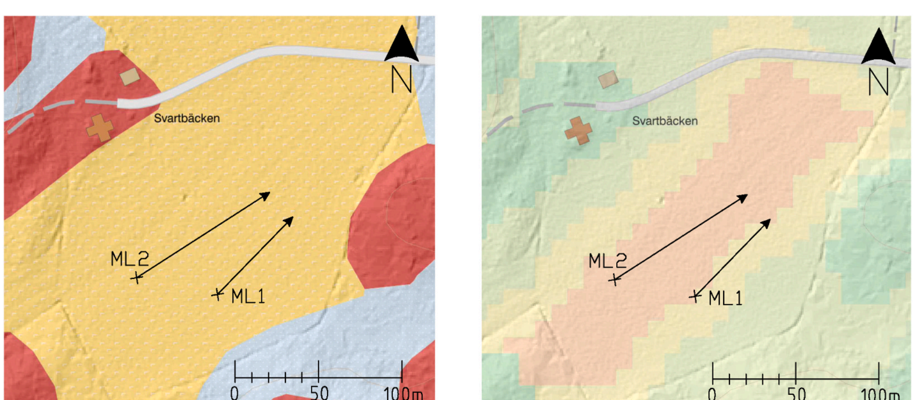

(a) (b)

Fig. 2. Geological maps of (a) soil types at the site with colors indicating post-glacial clay (yellow), till (blue) and bedrock (red), and (b) soil depth with colors corresponding to an estimated soil depth of 5–10 m (red), 3–5 m (yellow) and depths less than 1 m (green) [20]. The measurement lines ML1 and ML2 are superimposed for reference. (For interpretation of the references to color in this figure legend, the reader is referred to the Web version of this article.)

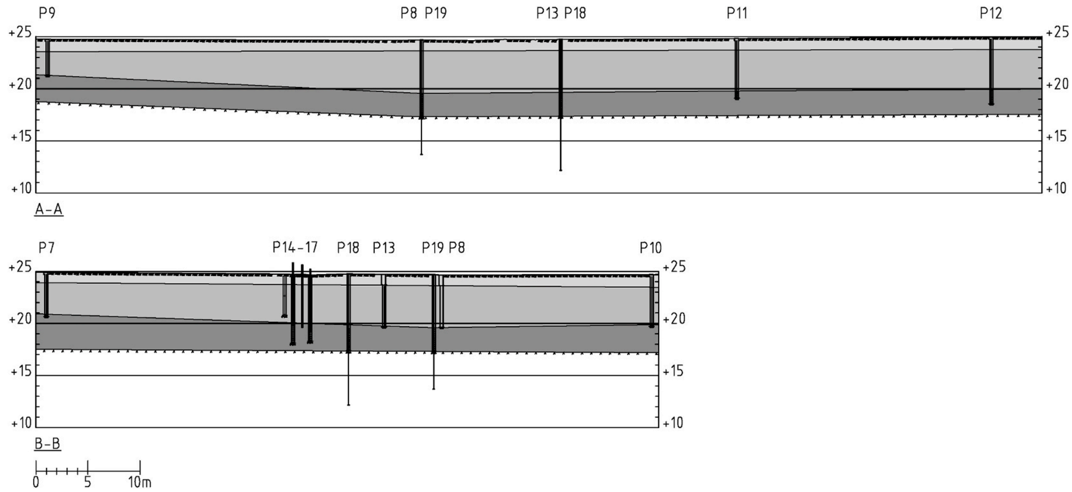

Fig. 3. Interpreted sections of the soil defined in Fig. 1 based on the information from the geotechnical site investigations. The investigation depth at each point is indicated and the interpreted layering of the soil is illustrated in shading as a dry-crust clay (top layer), soft clay (second layer) and till (third layer) on top of bedrock.

Fig. 4. Seismic cone penetration test equipment with two pre-loaded L-shaped plates, SCPT probe and a sledge hammer connected to the DAQ to trigger recording.

Table 1
Classification of the soil made by visual inspection according to ISO 14688–2:2017 [26].

Depth [m]	Soil classification
1	Sand infused slightly rusty brown **dry-crust clay**
2	Gray homogeneous **clay**
3	Sand infused lightly varved brown-gray **clay**
4	Lightly varved brown-gray **clay** with thin layers of silt
5	Sandy **gravel**

properties obtained from the laboratory measurements of the clay are presented in Table 2.

The triaxial apparatus and the oedometer housing were equipped with bender elements, allowing to perform measurements of the dilatational (P) and shear (S) wave speeds in the clay samples. The influence of anisotropy of the clay on the S-wave speed was investigated by performing measurements in both the axial and radial directions of the samples, corresponding to the vertical and horizontal in situ directions, respectively. The wave speed measurements in the axial direction were performed in a triaxial apparatus whereas the measurements of the wave speeds in the radial direction were performed in the oedometer using a radially oriented sample taken from the original piston sample by punching with the equipment presented in Fig. 5a, allowing to perform the analysis on standard size samples. The tests were performed with the samples re-loaded to in situ stresses.

The determination of wave speeds was limited to tests on two samples, one axially and one horizontally orientated, for samples collected at different levels. However, at the 2 m level the agreement between the wave speeds estimated from the two setups was evaluated by mounting an axially orientated sample in the oedometer. Table 3 presents a comparison of the results, indicating the consistency between the estimates obtained in oedometer and triaxial testing. Moreover, the axial wave speeds are compared to the radial ones at the in situ stress levels.

The results from the tests in the two perpendicular directions of the samples are presented in Table 4, indicating a structural anisotropy of the clay that varies with depth. However, for a horizontally stratified soil with vertical transverse isotropy (VTI), only the SH waves are affected by the S-wave speed anisotropy, while the P-SV waves are unaffected [28]. The anisotropy of the S-wave speeds is therefore disregarded in the remainder of this paper.

The material damping in the clay samples is estimated from the response signals generated from an axial excitation used to measure the P-wave speeds, applied as a single period of a sine at a frequency of 200 kHz. The damping is obtained using the Hilbert transform method recently introduced for material damping estimation from bender element tests by Cheng and Leong [29].

3.5. *Empirical correlations*

In literature, empirical correlations have been established for determining the initial shear modulus G_0 from index parameters used in geotechnical engineering. The international standard ISO 14837–32:2015 [30] gives an overview of methods for the evaluation of small-strain properties in soil, and lists the following two empirical

Table 2
Geotechnical parameters obtained from laboratory measurements on the clay piston samples from Brottby.

Depth	ρ	w	w_L	w_P	I_p	S_t	τ_{fu}^{triax}	τ_{fu}^{fc*}	OCR
[m]	[kg/m^3]	[%]	[%]	[%]	[%]	[–]	[kPa]	[kPa]	[–]
1	1880	31.8	59	–	–	–	54.4	>134.4	5**
2	1570	78.2	64	30	34	6	19.6	41.8	2.6
3	1720	53.6	49	20	29	15	19.2	16.0	1.9
4	1780	47.2	43	19	24	18	23.1	15.0	1.9

* Corrected with respect to the liquid limit according to Ref. [27].
** Estimated from CPT correlations.

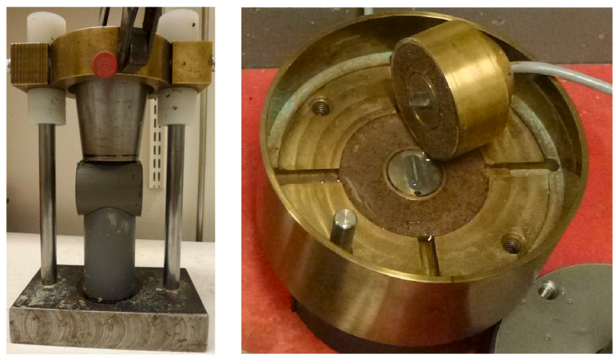

(a) (b)

Fig. 5. Laboratory preparation of (a) horizontal clay samples and (b) bender elements mounted in an oedometer housing.

Table 3
Comparison of measured S-wave speeds in samples collected at 2 m depth orientated in the axial and radial directions in triaxial and oedometer testing under different stress states.

Axial stress	$C_{s,a}$		$C_{s,r}$
	Triax	Oedometer	Oedometer
[kPa]	[m/s]	[m/s]	[m/s]
21.9		86.7	93.0
25.5	84.4	86.0	
27.9		86.5	93.6
54.0	88.9	89.0	

methods for the estimation of the initial shear modulus in cohesive soils.

The first method was established for Scandinavian clays by Larsson and Mulabdić [12]. The empirical relation is given by:

$$G_0 = \left(\frac{208}{I_p} + 250\right)\tau_{fu} \quad (1)$$

and is based on the plasticity index I_p (in decimals) and the undrained shear strength τ_{fu}. It should be noted that eq. (1) is restricted to the use of the undrained shear strength determined from a test that gives compatible results with the ones used for establishing the relation. The present relation is based on direct simple shear, dilatometer, corrected field vane and fall-cone tests [12].

In the second method, the initial shear modulus is estimated from empirical correlations established for CPT data. For cohesive soils, the initial shear modulus is estimated from [31]:

$$G_0(z) = p_a \frac{99.5}{e(z)^{1.13}}\left(\frac{q_t(z)}{p_a}\right)^{0.695} \quad (2)$$

where $p_a = 100$ kPa is a reference pressure, $e(z)$ is the void ratio as a function of the depth z and $q_t(z)$ is the corrected cone tip resistance. The correlation is based on data from a variety of different cohesive soils around the world, but predominantly on sites of soft Swedish clay with wave speeds determined from SCPT data [31]. The advantages of using the CPT data for estimating the initial shear modulus are the same as for the test in general, i.e. it provides a high resolution with depth and is based on in situ conditions. However, eq. (2) requires not only the results from the CPT, but also the variation of the void ratio with depth. At the present site, due to the full saturation of the clay below the dry crust, the void ratio can be estimated from:

$$e(z) = \frac{\rho(z)}{\rho_w(1 + 1/w(z)) - \rho(z)} \quad (3)$$

where ρ_w is the density of water, $\rho(z)$ is the soil density as a function of the depth z and $w(z)$ is the water content. As only point wise information is available of the clay density and water content, constant values of ρ and w obtained from Table 2 are assumed over each 1 m interval. The variation of the estimated S-wave speed with depth is subsequently

Table 4
Axial and radial effective stresses and S-wave speeds measured from triaxial test (axial) and oedometer test (radial) using bender elements.

Depth	σ'_a	σ'_r	$C_{s,a}$	$C_{s,r}$
[m]	[kPa]	[kPa]	[m/s]	[m/s]
1	59.0	46.0	139.0	162.4
2	25.5	21.9	84.4	93.0
3	32.3	24.0	89.4	85.9
4	40.0	26.0	95.1	86.7

calculated as:

$$C_s(z) = \sqrt{\frac{G_0(z)}{\rho(z)}} \tag{4}$$

4. Non-invasive site investigations

In addition to the invasive geotechnical tests by penetration of the soil, two active vibration measurements were performed along the measurement lines ML1 and ML2 in Fig. 1. The measurements along ML1 were conducted in the spring of 2019, while the measurements along ML2 were conducted in the autumn of the same year. The tests were performed by applying an impact force on the surface of the soil with an instrumented sledge hammer at the positions ($\times$) indicated in Fig. 1 and measuring the vertical acceleration responses along the lines extending from the excitation points.

4.1. Setup

The impact is generated at the soil's surface by hitting a 400 $\times$ 400 $\times$ 80 mm aluminium plate with an instrumented hammer of model Dytran 5803A IEPE with a mass of 5.5 kg, presented in Fig. 6a. The accelerations are measured by means of 30 uniaxial seismic accelerometers of models Colibrys SF1500S (ML1), PCB 393A01 and PCB 393B31 (ML2). The accelerometers are mounted on 300 mm long aluminium pickets with a cruciform cross section, measuring the response in the vertical direction. Fig. 6b presents an accelerometer mounted on a picket. The picket is designed to minimize soil-structure interaction effects in the frequency range of interest [32,33].

The measurements are performed in multiple setups, where the sensors are consecutively moved 0.5 m between each setup, achieving a sensor spacing along the measurement lines of $\Delta r = 0.5$ m.

The number of setups was 12 for ML1 using 10 accelerometers and 6 for ML2 using 30 accelerometers.

The first sensor is offset 0.5 m from the excitation point and the lengths of the measurement lines ML1 and ML2 are 60 and 90 m, respectively. In each setup, 80–100 impacts and the corresponding acceleration responses have been recorded for processing, to ensure a high confidence in the measured responses at the farthest receiver.

4.2. Post-processing

In order to suppress noise in the measurement data occurring due to ambient or distant external vibration sources, the average frequency response function $\widehat{H}_{ij}(\omega)$ between the free field acceleration channel i at distance r and the hammer force channel j is computed as a function of the circular frequency ω, using the H_1 estimator [34]:

$$\widehat{H}_{ij}(\omega) = \frac{\widehat{S}_{ij}(\omega)}{\widehat{S}_{jj}(\omega)} \tag{5}$$

with the average cross power spectral density between channels i and j defined as:

$$\widehat{S}_{ij}(\omega) = \frac{1}{N}\sum_{k=1}^{N} x_i^k(\omega) x_j^{k*}(\omega) \tag{6}$$

where N is the number of events, $x_i^k(\omega)$ is the Fourier transform of the time signal acquired for event k for channel i and $x_j^{k*}(\omega)$ is the complex conjugate of the transformed signal acquired for channel j.

The frequency response function estimate $\widehat{H}_{ij}(\omega)$ is based upon multiple observations, and can therefore be considered as a stochastic variable with a standard deviation $\widehat{\sigma}_{|H_{ij}|}(\omega)$. The relative statistical errors $\widehat{\sigma}_{|H_{ij}|}(\omega)/|H_{ij}(\omega)|$, or coefficient of variation (COV), on the estimated transfer function $\widehat{H}_{ij}(\omega)$ is given by [35]:

$$\mathrm{COV}_{ij} = \sqrt{\frac{1-\gamma_{ij}^2(\omega)}{2N\gamma_{ij}^2(\omega)}} \tag{7}$$

$$\gamma_{ij}^2(\omega) = \frac{\widehat{S}_{ij}(\omega)\widehat{S}_{ij}^*(\omega)}{\widehat{S}_{ii}(\omega)\widehat{S}_{jj}^*(\omega)} \tag{8}$$

where $\gamma_{ij}(\omega)$ is the coherence between channels i and j. Fig. 7 presents the estimated acceleration frequency response functions, or accelerances, as a function of distance for the two test setups along ML1 and ML2, along with the corresponding coefficient of variation. A low variation is found in the frequency band between 8 and 60 Hz that significantly contributes to the response at a given offset. As the source-receiver distance increases, the higher frequency waves are attenuated due to material damping leading to a lower signal to noise ratio and eventually no response is measurable for the highest frequencies considered, leading to a high variation in the estimates.

The estimated accelerances are transformed from the frequency-spatial domain to the frequency-wavenumber domain by applying the transformation [36]:

$$\widetilde{H}(k_r,\omega) = \frac{1}{2}\int_0^\infty \widehat{H}(r,\omega)H_0^{(1)}(k_r r)r\,\mathrm{d}r \tag{9}$$

where $\widehat{H}(r,\omega)$ are the estimated frequency response functions as a function of the radial distance r from the source point, k_r is the radial

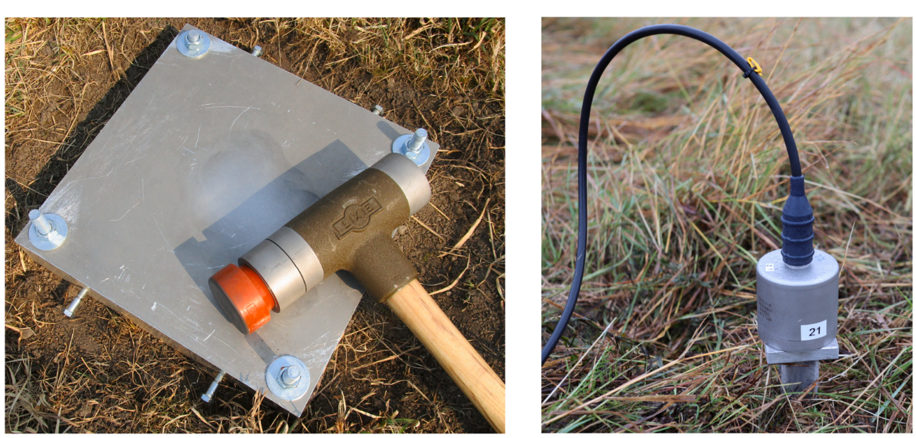

(a) (b)

Fig. 6. Experimental setup of (a) excitation point foundation and (b) accelerometer mounting.

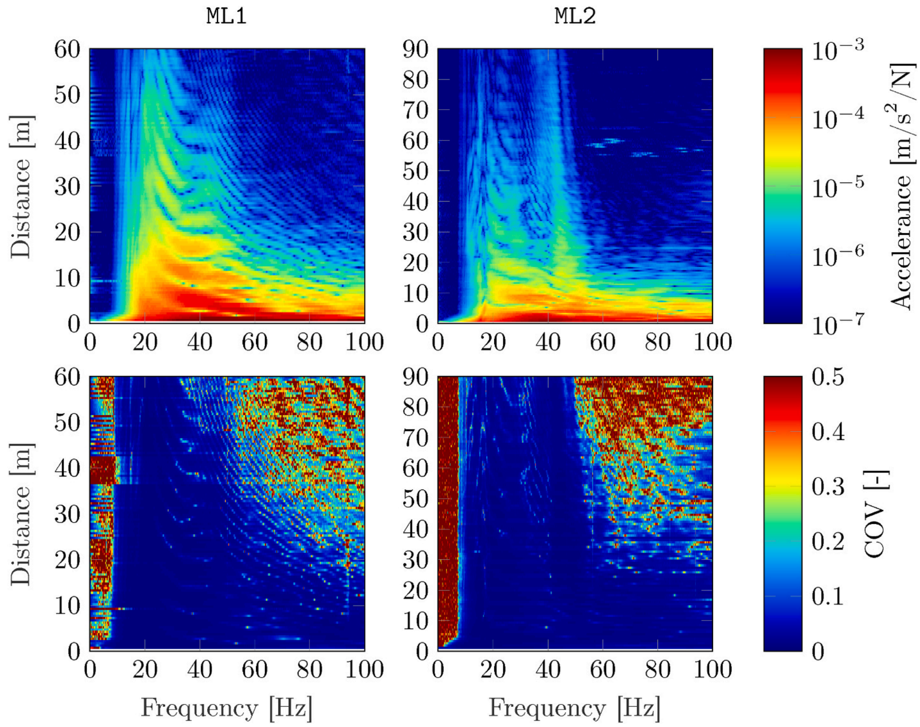

Fig. 7. Estimated accelerances and corresponding coefficients of variation for tests along measurement lines ML1 and ML2.

wave number and $H_0^{(1)}$ is the zero-th order Hankel function of the first kind. This transformation accounts for the cylindrical nature of the wave field when decomposing it into its plane wave components, and considers that the wave field consists solely of outing waves.

The integral of eq. (9) is numerically evaluated with a sampling of Δr corresponding to the distance in between the receivers and the integral is truncated at the array length. The evaluation of the integral is performed by the means of a generalized Filon quadrature scheme implemented in the Matlab toolbox EDT [37,38]. The resulting spectra are presented in Fig. 8 in terms of phase speed $C_r = \omega/k_r$ and frequency responses normalized for each frequency line.

4.3. Model inversion

The experimental measurements are subsequently post-processed to estimate the P- and S-wave speeds in the soil. The P-wave speeds are first estimated from a seismic refraction analysis based on the first arrival times at the receivers. The P- and S-wave speed, soil layer thickness and material damping ratios are subsequently obtained from a model inversion of the refraction, dispersion and attenuation curves. The dispersion curves of the surface waves are identified as peaks in the frequency-wavenumber spectra [39]. Surface waves attenuate due to both radiation and material damping. Material damping of surface waves results in a spatial decay of the surface waves proportional to $\exp(-A_n(\omega)r)$, where $A_n(\omega)$ is the attenuation coefficient of the associated surface wave mode n. The attenuation coefficients of the surface waves can be determined from the width of the peaks corresponding to the estimated dispersion curves. The half-power bandwidth and the circle fit method have been proposed as methods for estimating the attenuation coefficient from multiple dispersion curves [40,41]. Due to the presence of multiple dominant modes contributing to the response, apparent dispersion curves are determined by peak-picking in the frequency-phase speed spectra in Fig. 8 up to 60 and 46 Hz for ML1 and ML2, respectively. The attenuation curves are subsequently estimated using the half-power bandwidth method [40].

The theoretical dispersion and attenuation curves are obtained from the Green's functions for a horizontally layered soil on top of a halfspace computed using the direct stiffness method [42], which is a re-formulation of the Thomson-Haskell transfer matrix method [43,44]. The same soil model is used in section 6 to compute the free-field surface response. This is achieved by a Hankel transform of the Green's function from the frequency-wavenumber domain to the frequency-spatial domain which is implemented in the Matlab toolbox EDT [38]. The

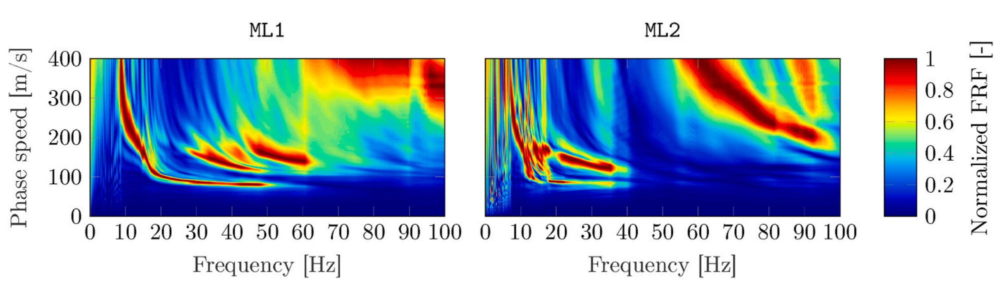

Fig. 8. Dispersion images normalized along each frequency line to the maximum value, for the tests along measurement lines ML1 and ML2.

assumption of a horizontally layered soil is justified based on the stratigraphy estimated from the soil investigations in Fig. 3, even if a small inclination of the layers is present [45].

The inverse problem is formulated as a non-linear least squares problem and is solved using a trust-region-reflective algorithm implemented in MATLAB [46], which is a local search method. Thereby, the problem suffers from non-uniqueness and the outcome strongly depends on the initial soil profile assumed. This is especially the case for soils that have an irregular variation of stiffness with depth [45]. Therefore, the initial soil profile is assigned considering the information available from the site investigations, including the stratification and the density of the clay. The densities of the till and bedrock were assumed as 2200 and 2700 kg/m^2, respectively. The initial S-wave speeds are heuristically obtained from the fundamental dispersion curve, relating the S-wave speed to the surface wave speed by $C_R = 1.1C_s$ and the representative depth as $z = \lambda_R/2.5$, with C_R and λ_R the surface wave speed and wavelength, respectively [47]. Due to the differences in the experimental dispersion curves, the soil properties of the profile obtained from the inversion along ML1 are used as an initial guess for the inversion along ML2, where the depth of the clay is adapted to be consistent with the observations made from the site investigations. Fig. 9 presents a comparison between the experimental dispersion and attenuation curves and the ones obtained from the inversion.

As the surface wave measurements cover a large portion of the soil, there is an inherent averaging over the distance covered by the measurement line. This can lead to differences between the identified profile from a model inversion and physical observations, as the inversion produces a horizontally layered soil model along the measurement line. Moreover, as the estimated profile is constructed by a discrete number of layers, averaging can occur over physical layer boundaries, especially when the stiffness contrast is low between the materials.

5. Synthesis of investigation results

Fig. 10 compares the S-wave speeds obtained from the empirical correlations with the ones obtained from the bender element, SCPT and SASW tests. The estimates from the CPT correlation agree closely with the results from the bender element tests and are also consistent with the SCPT results. Moreover, the variation in stiffness of the layers between 1 and 2 m predicted by both SASW tests are captured.

The empirical correlation of eq. (1) overestimates the S-wave speed in the upper 2 m of the soil but agrees with the other tests for the 3 and 4 m levels. Larsson and Mulabdić [12] noted that in comparison with SCPT results in Swedish clay, empirical relations tended to over-predict the initial shear modulus in the uppermost soil layers. For the present site, the estimated shear strengths obtained from the fall-cone and triaxial tests show large differences in the upper 2 m of the soil. In fact, employing the results obtained from the triaxial tests at the 1 and 2 m level yield, despite not being the basis for the empirical correlation, a better estimation of the S-wave speeds in line with the other tests. However, at the deeper levels the opposite holds demonstrating the significant influence of the chosen method to determine the shear strength on the estimated wave speeds.

For P13, a large scatter in the SCPT estimates obtained from the two setups is found in the upper 1.5 m of the soil. Generally, the upper part of a soil profile is not accurately estimated in the SCPT due to the small effective spacing of the sensors, even for synthetic signals [48]. Moreover, large amplitude impacts at the surface can induce shear strains in clays that are outside the range where the soil can be considered linear, violating the assumed test conditions [12]. Therefore, the results from the SCPT in the uppermost 1.5 m of the soil are considered less reliable.

It should be noted that none of the invasive methods to estimate the material wave speeds provide information of the top 1 m of the soil or the underlying till and bedrock. This is due to the practical limitations of the methods. Undisturbed samples were not practically attainable in the uppermost meter of the soil and the sampling is only applicable for the clay, as is the CPT and SCPT. In contrast, the surface wave methods provide estimates in the regions not covered by the invasive tests. The results indicate a significantly lower S-wave speed in the upper 0.8 m compared to the underlying layer, and provide estimates of the wave speeds in the till and the bedrock. Along ML1, a stiffer layer is estimated to be located closer to the surface than along ML2, agreeing with the observations made from the geotechnical site investigations, cf. Figs. 3 and 10. This emphasises the importance of considering the propagation path of interest for determining the soil properties by model inversion, as the stratification and layer depths affect the character of the wave propagation in the soil. However, the discrepancy between the estimated S-wave speeds in the till is large and should not be considered as the true material property, but rather as an effective value describing the wave propagation along the measurement line. The depth to bedrock is overestimated by the SASW test along ML2 compared to the physical observations. This is caused by the computed dispersion curve becoming insensitive to the position of the bedrock in the optimization problem.

Fig. 11 presents the P-wave speeds estimated from the two SASW and from the laboratory bender element tests.

The SASW tests estimate the P-wave speed in the upper meter of the soil to be significantly lower than the underlying soil, especially for the test along ML2. As the clay becomes saturated, the P-wave speed approaches the speed of sound in water and the Poisson's ratio becomes close to 0.5. It was observed during the site investigations that the clay is saturated at approximately 1 m below the surface. This is supported by the results from the bender element tests, indicating a P-wave speed in the clay of approximately 1200 m/s. The lower values obtained from the model inversions at depths below 2 m are therefore considered as inaccurate.

The material damping ratios estimated from the two model inversions agree closely, where the material damping ratios in volumetric (β_p) and deviatoric deformation (β_s) are assumed to be equal. The damping ratios β_p in the clay estimated from the P-wave bender element tests at the 2, 3 and 4 m depths are consistent with each other and

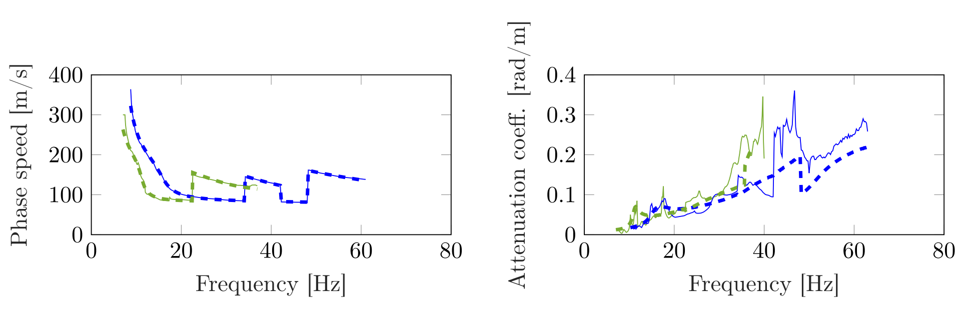

Fig. 9. Comparison of experimental (solid lines) and model (dashed lines) (a) dispersion and (b) attenuation curves for ML1 (blue) and ML2 (green). (For interpretation of the references to color in this figure legend, the reader is referred to the Web version of this article.)

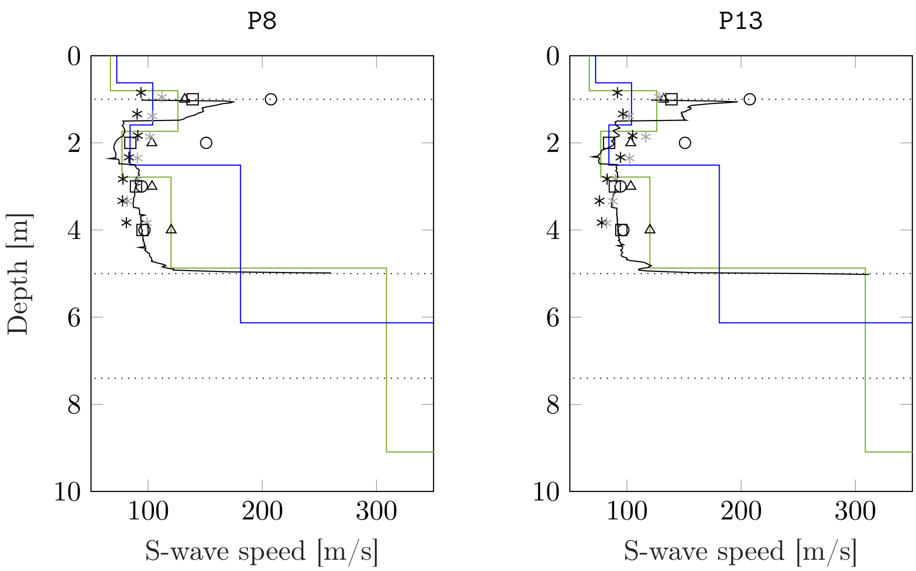

Fig. 10. S-wave speeds in points P8 and P13 estimated from empirical CPT correlation (black line) and SCPT (*) by hammer blows in the front (gray) and back (black) of the drill rig and observed layer boundaries (dotted lines). Estimates from SASW along ML1 (blue line) and ML2 (green line), empirical relation based on the shear strength from fall cone (○) and triaxial tests (△), and bender element laboratory tests in the vertical direction (□) obtained from samples taken at P13 are included for comparison. (For interpretation of the references to color in this figure legend, the reader is referred to the Web version of this article.)

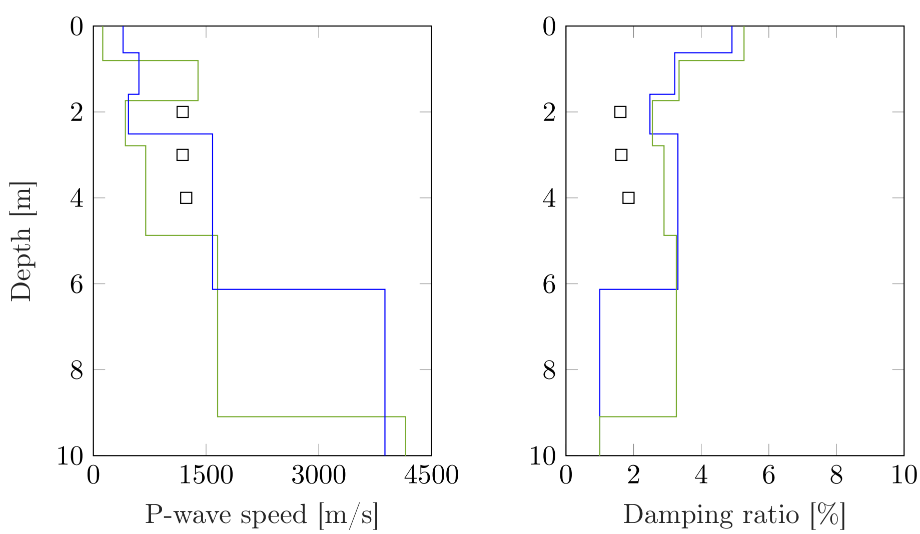

Fig. 11. P-wave speeds and material damping ratios estimated from SASW test along ML1 (blue line), ML2 (green line) and from bender element P-wave measurements estimated with the Hilbert transform method (□). (For interpretation of the references to color in this figure legend, the reader is referred to the Web version of this article.)

present lower values of the material damping compared to the ones obtained from the SASW tests. To accurately account for material damping becomes increasingly important with source-receiver distance, and is therefore especially relevant for predictions at significant distances with respect to the wavelengths of the propagating waves.

As the points P8 and P13 where the point wise investigations are performed are positioned along ML2, and the estimated profile obtained from the SASW test is in good agreement with the site observations, a representative layered soil model is assembled by synthesis of the estimated material parameters along ML2. Table 5 presents a summary of the soil properties synthesised from the tests. The P-wave speed of the top layer is inconsistently estimated from the two SASW tests carried out in different seasons and the difference in the estimated material damping ratios in the clay is significant. The influence of these material properties and seasonal variations on the surface response is therefore investigated next.

Table 5
Small-strain soil properties estimated for the soil profile along ML2 synthesised from the investigations.

Layer	Depth	h	C_s	C_p	β_s	β_p	ρ
	[m]	[m]	[m/s]	[m/s]	[–]	[–]	[kg/m^3]
1	0.80	0.80	67	125	0.053	0.053	1880
2	1.73	0.93	126	1200	0.017	0.017	1570
3	2.78	1.05	77	1200	0.017	0.017	1720
4	4.87	2.09	120	1200	0.017	0.017	1780
5	7.4	2.53	309	1654	0.033	0.033	2200
6	∞	∞	2236	4156	0.010	0.010	2700

6. Validation and physical interpretation

The synthesised model is validated against the measured frequency response functions along ML2. The comparison is made in terms of velocities and mobilities, where the mobilities are obtained from the accelerance by divsion with iω.

To facilitate a comparison in the time domain, the computed and measured mobilities are subjected to an artificial band-limited impact load of similar character as employed in the measurements. The time- and frequency domain representations of the load are presented in Fig. 12.

6.1. Properties of the top soil layer

The estimated depths and S-wave speeds of the top soil layer are consistently estimated in the two SASW tests. However, the estimated P-wave speed differs substantially between the measurements. The influence on the computed response is therefore investigated by considering the P-wave speed of the first layer in Table 5 equal to the value $C_{\mathrm{p1}} =$ 395 m/s estimated from the SASW test along ML1.

Fig. 13 presents a comparison between experimental and computed mobilities, and time domain responses due to the impact load along ML2 at 30, 50, 70 and 90 m distance from the source.

The increased P-wave speed results only in slight differences for frequencies below 30 Hz at larger distances, while the responses predicted by the synthesised soil model at frequencies between 30 and 50 Hz are almost entirely absent. The time domain representation illustrates that this frequency content is related to the first arriving group of waves, which is also validated by the responses obtained from the measurement data. Fig. 7 in section 4.2 shows the measured accelerances along ML2. It presents a consistent peak in this frequency band showing, with a higher spatial resolution, a slow attenuation with distance and how this response is almost unaffected by wave interference at distances larger than 40 m.

Fig. 14 presents a comparison of the numerical and experimental mobility-frequency-phase speed spectra along ML2.

The synthesised soil model captures the relatively large contribution of dispersion curves with phase speeds higher than 1000 m/s at frequencies above 30 Hz in the spectrum obtained from the measurements. Assuming a higher P-wave speed in the top layer results, on the other hand, in a spectrum without this dispersion curve. The cut-off frequency of the dispersion curve associated with the P-wave speed of the first layer observed in Fig. 14 coincides with the resonance frequency of the fundamental eigenmode for vertically propagating P-waves of the top soil layer built in at its base $f_1 = C_{\mathrm{p1}}/(4h_1) = 39$ Hz, with C_{p1} and h_1 the P-wave speed and thickness of the first layer, respectively. This is due to the high P-wave speed contrast between the top layer and the underlying ones. Moreover, Fig. 14 provides an indication of the wave speeds associated with the resonant response of the top layer. Higher frequency surface waves are generally attenuated more rapidly with distance compared to lower frequency waves due to material damping, as the effective attenuation is inversely proportional to the wavelength. However, the surface response observed above 30 Hz is not caused by a classical surface wave, but is a resonant response of the top layer due to P-waves refracted back towards the surface. P-waves that are critically refracted along the underlying layers travel at significantly higher speeds, and therefore with longer wavelengths, explaining the slow attenuation with distance in this frequency range. This phenomenon is further analysed in section 6.4.

To provide an overview of the topmost soil layer's influence on the attenuation with distance, the mobilities are represented in one-third-octave band spectra. Fig. 15 presents a comparison between sensors spaced by 5 m between 30 and 90 m source-receiver offset along the measurement line ML2, corresponding to distances longer than three wavelengths of the surface waves. Comparing Fig. 15a–c, it is evident that the slow attenuation with distance for the bands with center frequencies 31.5 and 40 Hz is only captured by the model where the top layer is present.

6.2. Elastic versus rigid bedrock

As the critically refracted body waves are amplified whenever the resonant frequency of the top layer falls within the frequency range of interest, considering the elasticity of the bedrock becomes important. As the bedrock is very stiff, a common assumption in modelling situations is to consider the bedrock as a rigid stratum. Fig. 16 presents a comparison of the responses computed at a 90 m source-receiver offset assuming the bedrock as an elastic halfspace and as rigid.

The response is identical at the lower frequencies associated with the surface waves. However, due to the lack of a bottom interface where waves are critically refracted, a substantially lower response is observed for higher frequencies when assuming the bedrock as a rigid stratum, demonstrating that this assumption cannot be motivated under the investigated soil conditions whenever larger source-receiver distances are of interest.

6.3. Material damping in the clay

The bender element tests are conducted on a very small specimen of the soil and at a much higher frequency than the range of interest, while the SASW tests yield estimates of the material damping based on data obtained over a larger body of soil and in situ conditions, but are sensitive to non-uniqueness. Therefore, the estimated values are uncertain and their influence on the predicted responses is investigated. Figs. 17 and 18 present a comparison between the measurements and the computed responses at the center and endpoints of ML1 and ML2, assuming the material damping in the clay according to the results from the bender elements test and the SASW inversions.

The model predictions assuming a material damping in the clay derived from the bender element tests yield more accurate predictions of amplitudes of the surface waves along both measurement lines, while the higher frequency content related to the refracted P-waves is less affected. These results suggest that reasonable estimates of damping values in homogeneous clays for performing vibration predictions can be obtained from bender element tests performed on standard size samples. However, further research is needed to confirm this conclusion.

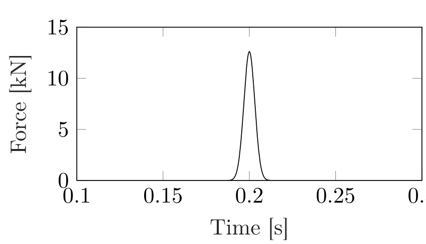

(a)

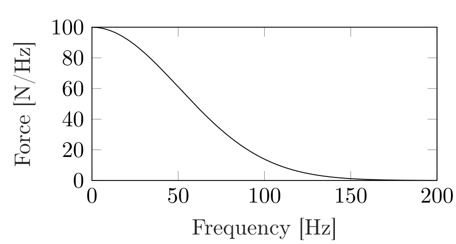

(b)

Fig. 12. Time-shifted Gaussian distribution applied as artificial impact load, (a) time and (b) frequency domain representation.

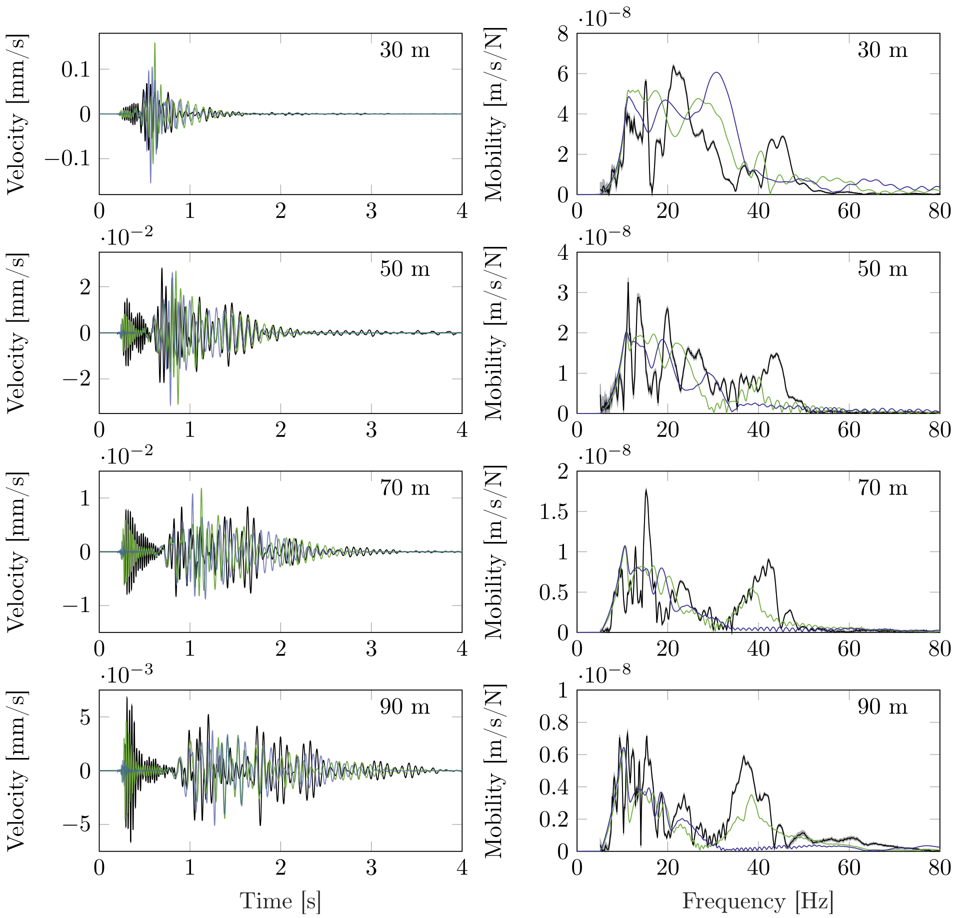

Fig. 13. Comparison of experimental and model results of time domain velocity responses due to a simulated impact (left) and mobilities (right) at 30, 50, 70 and 90 m from the source point along ML2. Responses are obtained from measurements (black) with 95% confidence bounds indicated, the synthesised soil model (green) and a soil model with an increased top layer P-wave speed (blue). (For interpretation of the references to color in this figure legend, the reader is referred to the Web version of this article.)

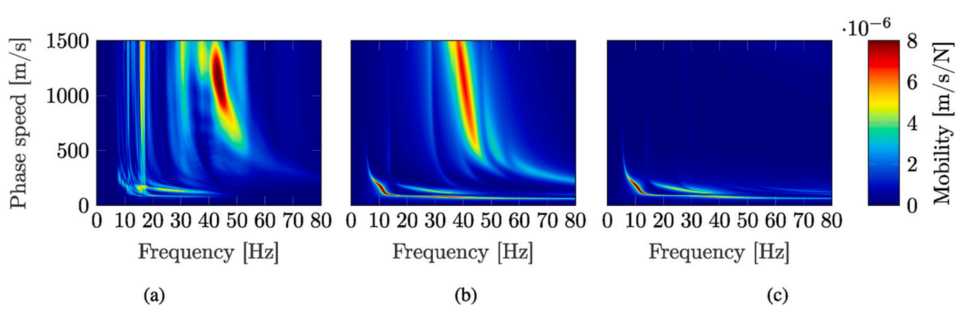

Fig. 14. Comparison of mobility-frequency-phase speed spectra along ML2 obtained from (a) measurements, (b) soil model with $C_{p1} = 125$ m/s and (c) soil model with $C_{p1} = 395$ m/s.

6.4. *Sensitivity analysis of soil layer properties*

Sections 6.1 and 6.2 compared the measured and computed surface responses and demonstrated the influence of the elastic properties of the dry top layer and the bedrock on the predicted response at the site. Schevenels et al. [49] showed that the layering introduced by the presence of the groundwater table in an otherwise homogeneous soil results in the existence of wave reflections, critically refracted waves and standing P-waves in the dry layer that influence the surface response. At the test site investigated in this paper, a large amplification is observed for the frequencies where standing P-waves develop in the dry layer due to the existence of a shallow bedrock with significantly higher material wave speeds than the soil.

In the following, the influence of soil layer thicknesses and the bedrock stiffness on the surface response is addressed to demonstrate the relevance of the observed phenomenon for sites with similar soil conditions. The soil profile identified for the test site is aimed at representing as closely as possible the dynamic behaviour of the soil. However, to facilitate understanding of the system, a simplified three layer model is considered to more clearly highlight the influence of the layering. Table 6 presents the soil properties assumed for the three layer soil model under consideration.

Four cases of parameter variations are considered to demonstrate the influence on the computed mobilities at a 90 m source-receiver offset. In order to avoid confounding, material damping ratios of all layers are set equal. In all cases where the P-wave speed is altered, Poisson's ratio is kept constant and the S-wave speed is changed accordingly.

First, the thickness of the top soil layer is investigated. Fig. 19a presents the effect of increasing only the thickness of the top layer, demonstrating the direct influence it has on the response with peaks

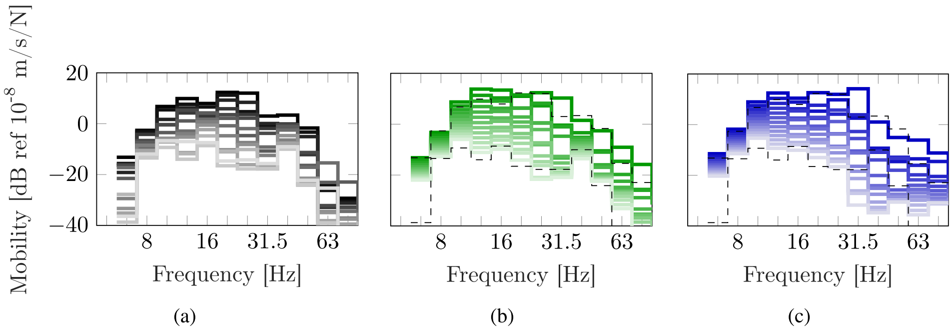

Fig. 15. One-third-octave band spectra for 13 equidistant points between 30 and 90 m source-receiver offset (dark to light) obtained from (a) measurements along ML2, (b) the synthesised soil model and (c) the soil model assuming $C_{p1} = 395$ m/s. The envelope of the measurements is superimposed on the simulation results for comparison (black dashed lines).

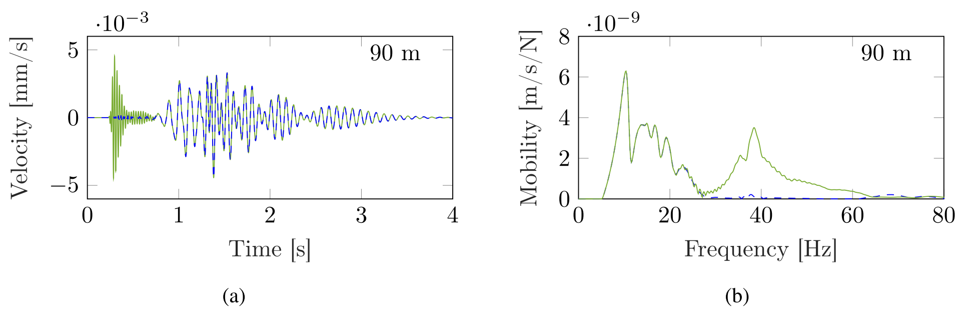

Fig. 16. Comparison of simulated (a) time domain velocity responses due to an impact load and (b) mobilities at 90 m from the source point assuming the bedrock as elastic (green) and as rigid (blue). (For interpretation of the references to color in this figure legend, the reader is referred to the Web version of this article.)

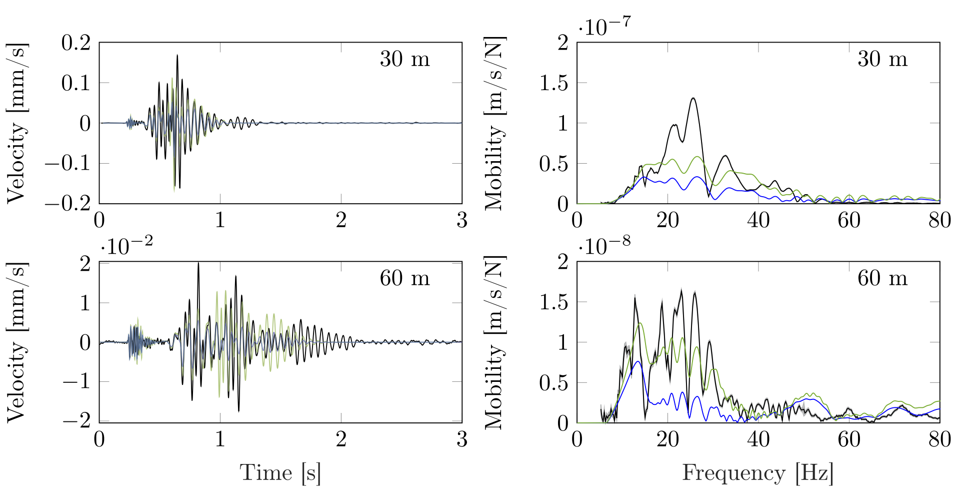

Fig. 17. Comparison of experimental and model results of time domain velocity responses due to a simulated impact (left) and mobilities (right) at the center and endpoint of ML1. Responses are obtained from measurements (black) with 95% confidence bounds indicated, a soil model assuming damping values in the clay obtained from bender element tests (green) and from the SASW inversions (blue). (For interpretation of the references to color in this figure legend, the reader is referred to the Web version of this article.)

corresponding to the resonance frequencies of a layer built in at its base $f_n = C_{p1}/4h_1(2n-1)$. Fig. 19b shows the influence of the same variation of layer thickness but with a constant resonance frequency of the top layer by adjustment of the P-wave speed. In contrast to Fig. 19a, the resonance peaks occur at the same frequency but present different amplitudes. This is due to the increase of the mass in the top layer with an increasing layer thickness, causing a reduction in amplitude of the layer resonance.

Second, the influence of increasing the depth of the saturated clay layer is illustrated in Fig. 20a, showing that as the layer thickness increases the resonance in the top layer remains present and no significant decrease of magnitude is observed for the considered depths and source-receiver distance. Third, Fig. 20b shows the influence of the bedrock wave speed. When the P-wave speed of the bedrock is equal to that of the saturated soil, the resonance peak diminishes. On the other hand, when refraction in the bedrock is possible the response of the top layer is significant, demonstrating the contribution from refracted waves to the total response in this frequency range.

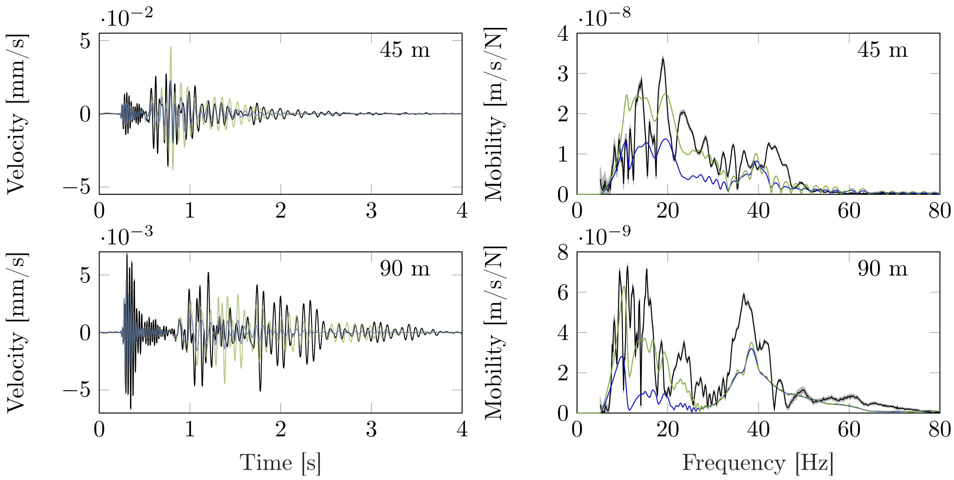

Fig. 18. Comparison of experimental and model results of time domain velocity responses due to a simulated impact (left) and mobilities (right) at the center and endpoint of ML2. Responses are obtained from measurements (black) with 95% confidence bounds indicated, the synthesised soil model (green) and a soil model assuming damping values from the SASW inversions (blue). (For interpretation of the references to color in this figure legend, the reader is referred to the Web version of this article.)

Table 6
Small-strain soil properties of a simplified three layer model used for sensitivity analysis.

Layer	h [m]	C_s [m/s]	C_p [m/s]	β_s [−]	β_p [−]	ρ [kg/m^3]
1	0.80	70	125	0.03	0.03	1700
2	7	90	1200	0.03	0.03	1700
3	∞	2000	3600	0.03	0.03	2700

7. Seasonal variations

In the measurements, the response associated with the uppermost soil layer is not as pronounced along ML1 as along ML2, and the SASW along ML1 leads to a higher estimated P-wave speed than along ML2. It is here noted that the tests were performed along ML1 in the spring under dry conditions and along ML2 in the autumn under wet conditions with a higher moisture content in the soil at the surface. This leads to the hypothesis that seasonal variations affect the mechanical properties, and therefore the dynamic response, of the soil. Additional measurements have been performed at the site at different occasions and during different seasons. The temperature was not below 0 °C and there was no freezing of the soil at any of the occasions. Fig. 21 presents the response at point P10 due to a load applied at P8, with reference to Fig. 1 in section 2. The excitation was applied to a 0.5 × 0.5 × 0.2 m cast-in place concrete foundation and the sensor mount was left in place in between the measurements. The response at lower frequencies is unaltered in between the measurements, while for frequencies above 20 Hz, a

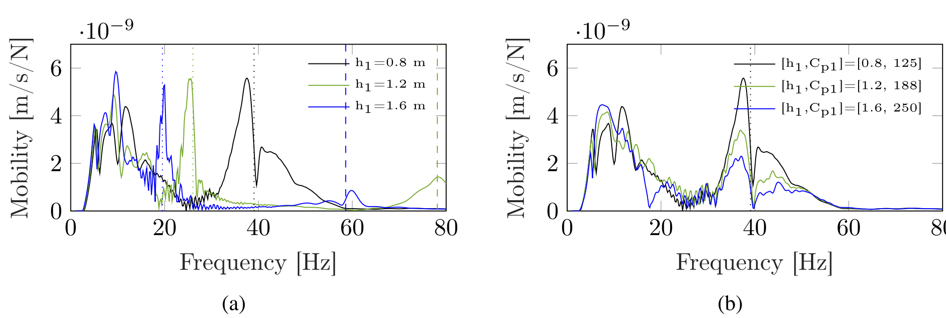

Fig. 19. Mobilities at the soil's surface at 90 m source-receiver distance assuming (a) different values of the top layer thickness and (b) adjusting the P-wave speed accordingly to obtain the same layer resonance frequency. The first (vertical dotted lines) and second (vertical dashed lines) layer resonance frequencies of a layer built in at it's base are indicated.

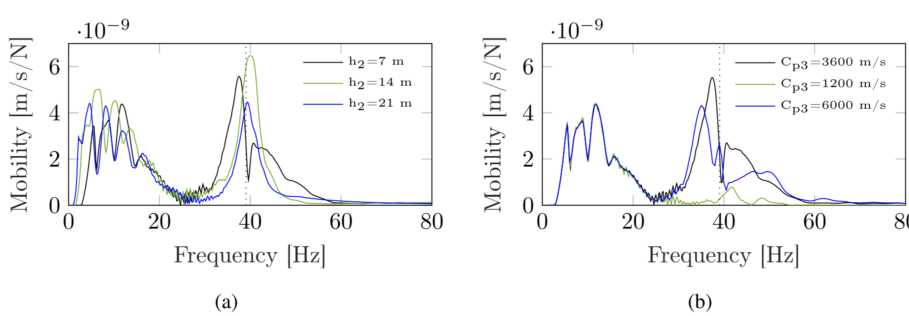

Fig. 20. Mobilities at the soil's surface at 90 m source-receiver distance assuming (a) different depths of the saturated clay and (b) different P-wave speeds of the elastic bedrock. The first layer resonance frequency (vertical dotted line) of a layer built in at it's base is indicated.

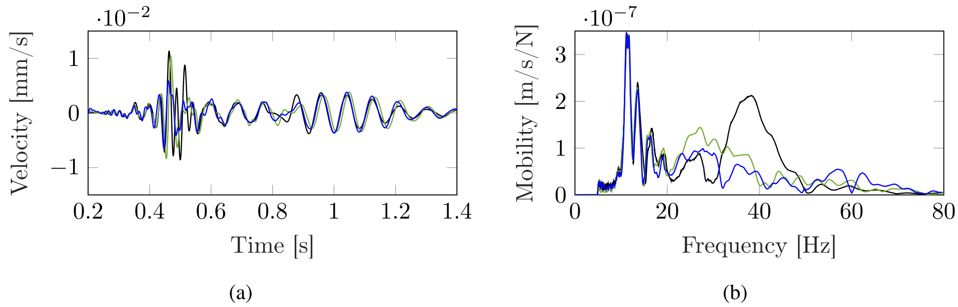

Fig. 21. Measurements performed in November (black), June (dark gray) and September (light gray) between points P8 and P10 presented as (a) time domain velocity responses due to an impact load and (b) mobilities.

difference in the response is observed between all three measurements. These observations show that seasonal variations change the dynamic response of the soil in this frequency range, associated with the resonance of the top layer treated in section 6.1 and more shallow penetration depths of the surface waves. Possible explanations for the observed variations are the moisture in the top part of the soil, closing micro fissures in the dry crust, and variation of the depth to where the clay becomes fully saturated. The ground water level was measured in the underlying non-cohesive soil at the time of each measurement, with reference to the ground surface. The ground water level varied from 1.75 m in November to 0.65 and 0.85 in June and September, respectively. As the depth to the saturated clay governs the resonance frequency of the top layer, the depth to the saturated clay is a possible explanation for the observed variations.

8. Conclusion

This paper presents an extensive site characterization of a Swedish clay deposit by geotechnical and seismic measurements to estimate material wave speeds and material damping in the soil for the prediction of environmental vibrations using a layered soil model. The soil conditions at the test site consist of a shallow soft clay underlain by till and a stiff bedrock. The stratigraphical layout over the area of investigation is estimated based on geotechnical site investigations whereas the soil is characterised from laboratory analyses of piston samples. Estimation of the wave speeds in the soil are obtained from empirical relations, bender element measurements in the vertical and horizontal directions, SCPT and two active surface wave measurements. The surface wave measurements are used to perform refraction analyses and model inversions of dispersion and attenuation curves (SASW), allowing to estimate layer thicknesses, material wave speeds and damping ratios.

The S-wave speeds estimated in the clay by SASW, SCPT, CPT empirical correlations and bender element tests are consistent while the empirical relation based on the shear strength derived from the fall-cone test and the plasticity index overestimates the wave speeds in the upper 2 m of the soil. CPT correlations provide satisfactory estimates for the S-wave speed in the clay under the studied conditions, and yield the most accurate estimation of S-wave speeds in the soil whenever dynamic measurements are unavailable. The material damping ratios of the soil are estimated from two SASW tests yielding consistent results, and from the free vibration of samples excited in axial motion using bender elements, yielding lower values for the saturated clay. It is demonstrated that the material damping measured in the laboratory leads to a closer agreement between predicted and measured responses for the identified soil profile.

Only the surface wave measurements are able to provide estimates of the wave speeds in the top part of the soil, the till underlying the clay and the bedrock. The estimated properties of the uppermost soil are found to have a profound influence on the vertical surface response in a narrow frequency band related to the fundamental resonance frequency of the upper soil layer for vertically propagating P-waves, especially with an increasing source-receiver distance. This is caused by the large P-wave speed contrast between the topmost part of the soil and the underlying fully saturated clay. Model investigations demonstrate that the observed resonance peak is caused by the critically refracted P-waves along the interfaces of the underlying layers of soil and the elastic bedrock, resulting in a slow attenuation with distance due to the long wavelengths involved. The observed resonance effect is found, however, to be of varying magnitude when measured during different seasons, suggesting that seasonal variations can have an influence on the properties of the topmost soil and therefore also on the soil's dynamic surface response.

Author statement

The experimental and numerical works as well as the writing of the paper have been performed by the first author. The other authors contributed in the planning of the work, the discussion about the results and the reviewing of the paper.

Declaration of competing interest

The authors declare that they have no known competing financial interests or personal relationships that could have appeared to influence the work reported in this paper.

Acknowledgements

This work was supported by the Swedish Building, Development and Research fund (SBUF). The funding for experiments and site investigations was received from Vinnova, the Richertska foundation and Trafikverket. The financial support is gratefully acknowledged. The authors would like to thank the Swedish Geotechnical Institute (SGI) and Martin Holmén for providing the laboratory analysis of the soil samples. Freddie Theland would like to acknowledge the help of Lola Martínez-Rodrigo, Stefan Trillkott, Abbas Zangeneh and Andréas Andersson in conducting the dynamic site measurements. Finally, the authors would like to extend their gratitude towards Ragnvald Andersson for granting unlimited access to the test site used in this work.

References

[1] Lombaert G, Degrande G, Clouteau D. The influence of the soil stratification on free field traffic-induced vibrations. Arch Appl Mech 2001;71:661–78.
[2] Kouroussis G, Conti C, Verlinden O. Investigating the influence of soil properties on railway traffic vibration using a numerical model. Veh Syst Dyn 2013;51:421–42.
[3] ISO 14837-1:2005. Mechanical vibration – ground-borne noise and vibration arising from rail systems – Part 1: general guidance, Standard. Geneva, CH: International Organization for Standardization; 2005.
[4] Hanson CE, Ross JC, Towers DA. High-speed ground transportation noise and vibration impact assessment, technical report. Federal Railroad Administration; 2012.

[5] Connolly D, Marecki GP, Kouroussis G, Thalassinakis I, Woodward P. The growth of railway ground vibration problems - a review. Sci Total Environ 2016;568: 1276–82.
[6] Lombaert G, Degrande G, Kogut J, François S. The experimental validation of a numerical model for the prediction of railway induced vibrations. J Sound Vib 2006;297:512–35.
[7] Kouroussis G, Verlinden O, Conti C. Free field vibrations caused by high-speed lines: measurement and time domain simulation. Soil Dynam Earthq Eng 2011;31: 692–707.
[8] Connolly D, Alves Costa P, Kouroussis G, Galvin P, Woodward P, Laghrouche O. Large scale international testing of railway ground vibrations across europe. Soil Dynam Earthq Eng 2015;71:1–12.
[9] Bahrekazemi M. Train-induced ground vibration and its prediction. Ph.D. thesis, KTH Royal Institute of Technology; 2004.
[10] Hunaidi O, Tremblay M. Traffic-induced building vibrations in Montréal. Can J Civ Eng 1997;24:736–53.
[11] Svensson M, Möller B. Geophysics in soil mechanics - in situ shear moduli determined by SASW-technique and more traditional geotechnical methods, Technical Report. SGI - Swedish Geotechnical Institute; 2001.
[12] Larsson R, Mulabdić M. Shear moduli in Scandinavian clays. Measurement of initial shear modulus with seismic cones. Empirical correlations for the initial shear modulus in clay,. Swedish Geotechnical Institute; 1991. Technical Report 40.
[13] Wood T. On the small strain stiffness of some scandinavian soft clays and impact on deep excavations. Chalmers University of Technology; 2016. PhD. thesis.
[14] Adolfsson K, Andréasson B, Bengtsson P-E, Bodare A, Madshus C, Massarsch K, Wallmark G, Zackrisson P. High speed lines on soft ground. Evaluation and analyses of measurements from the West Coast Line Part 1-2. Banverket: Technical Report; 1999.
[15] Madshus C, Kaynia A. High-speed railway lines on soft ground: dynamic behaviour at critical train speed. J Sound Vib 2000;231:689–701.
[16] Hall L, Bodare A. Analyses of the cross-hole method for determining shear wave velocities and damping ratios. Soil Dynam Earthq Eng 2000;20:167–75.
[17] Hall L. Simulations and analyses of train-induced ground vibrations in finite element models. Soil Dynam Earthq Eng 2003;23:403–13.
[18] Paolucci R, Maffeis A, Scandella L, Stupazzini M, Vanini M. Numerical prediction of low-frequency ground vibrations induced by high-speed trains at Ledsgaard, Sweden. Soil Dynam Earthq Eng 2003;23:425–33.
[19] Google Earth Pro V.7.3.3.7786. Brottby, Sweden, march 19, 2020. 59°35'24.3"N 18°10'26.0"W, eye alt 383 m. Maxar Technologies. http://www.earth.google.com. [Accessed 21 September 2020].
[20] SGU. Map viewer, 21; 2020. p. 2020. Retrived September.
[21] SGF, Geoteknisk fälthandbok. Technical report. Swedish Geotechnical Society; 2013.
[22] ISO 22476-15:2016. Geotechnical investigation and testing – field testing – Part 15: measuring while drilling. Geneva, CH: Standard, International Organization for Standardization; 2016.
[23] Areias L, Van Impe FW. Effect of travel path in the SCPT test method. In: GeoShanghai International Conference; 2006. p. 236–42.
[24] ISO 22475-1:2006. Geotechnical investigation and testing – sampling methods and groundwater measurements – Part 1: technical principles for execution, Standard. Geneva, CH: International Organization for Standardization; 2006.
[25] ISO 14688-1:2017. Geotechnical investigation and testing – identification and classification of soil – Part 1: identification and description, Standard. Geneva, CH: International Organization for Standardization; 2017.
[26] ISO 14688-2:2017. Geotechnical investigation and testing – identification and classification of soil – Part 2: principles for a classification, Standard. Geneva, CH: International Organization for Standardization; 2017.
[27] Larsson R, Sällfors G, Bengtsson P-E, Alén C, Bergdahl U, Eriksson L. Skjuvhå llfasthet - utvärdering i kohesionsjord. Swedish Geotechnical Institute; 2007. Technical Report 3.
[28] Park J, Kaynia AM. Stiffness matrices for fluid and anisotropic soil layers with applications in soil dynamics. Soil Dynam Earthq Eng 2018;115:169–82.
[29] Cheng Z, Leong E. Determination of damping ratios for soils using bender element tests. Soil Dynam Earthq Eng 2018;111:8–13.
[30] ISO 14837-32:2015. Mechanical vibration – ground-borne noise and vibration arising from rail systems – Part 32: measurement of dynamic properties of the ground, Standard. Geneva, CH: International Organization for Standardization; 2015.
[31] Mayne PW, Rix GJ. $G_{\mathrm{max}} - q_c$ relationships for clays. Geotech Test J 1993;16: 54–60.
[32] Hunaidi O, Rainer JH. Evaluation of measurement limits of transducer mountings in the ground. Canadian Acoustics; 1990.
[33] Degrande G, Van den Broeck P, Clouteau D. A critical appraisal of in situ vibration measurements. 3rd European conference in structural dynamics. Florence: Balkema; 2014. p. 1107–16.
[34] Heylen W, Lammens S, Sas P. Modal analysis theory and testing, division of production engineering, machine design and automation. Katholieke Universiteit Leuven; 1994.
[35] Bendat J. Statistical errors in measurement of coherence functions and input/output quantities. J Sound Vib 1978;59:405–21.
[36] Forbriger T. Inversion of shallow-seismic wavefields: I. Wavefield transformation. Geophys J Int 2003;153:719–34.
[37] Frazer LN, Gettrust JF. On a generalization of Filon's method and the computation of the oscillatory integrals of seismology. Geophys J Roy Astron Soc 1984;76: 461–81.
[38] Schevenels M, François Stijn, Degrande G. EDT: an ElastoDynamics toolbox for MATLAB. Comput Geosci 2009;35:1752–4.
[39] Park CB, Miller RD, Xia J. Multichannel analysis of surface waves. Geophysics 1999;64:800–8.
[40] Badsar SA, Schevenels M, Haegeman W, Degrande G. Determination of the damping ratio in the soil from sasw tests using the half-power bandwidth method. Geophys J Int 2010;182:1493–508.
[41] Verachtert R, Lombaert G, Degrande G. Multimodal determination of Rayleigh dispersion and attenuation curves using the circle fit method. Geophys J Int 2017; 212:2143–58.
[42] Kausel E, Roësset JM. Stiffness matrices for layered soils. Bull Seismol Soc Am 1981;71:1743–61.
[43] Thomson WT. Transmission of elastic waves through a stratified solid medium. J Appl Phys 1950;21:89–93.
[44] Haskell NA. The dispersion of surface waves on multilayered media. Bull Seismol Soc Am 1953;43:17–34.
[45] Verachtert R. Deterministic and probabilistic determination of dynamic soil characteristics. KU Leuven, Department of Civil Engineering; 2017. PhD. thesis.
[46] MATLAB optimization toolbox, Matlab optimization toolbox. Natick, MA, USA: The MathWorks; 2019.
[47] Abbiss CP. Shear wave measurements of the elasticity of the ground. Geotechnique 1981;31:91–104.
[48] Karl L, Haegeman W, Degrande G. Determination of the material damping ratio and the shear wave velocity with the seismic cone penetration test. Soil Dynam Earthq Eng 2006;26:1111–26.
[49] Schevenels M, Degrande G, Lombaert G. The influence of the depth of the ground water table on free field road traffic-induced vibrations. Int J Numer Anal Methods GeoMech 2004;28:395–419.